JOURNAL OF AIRCRAFT
Vol. 46, No. 3, May–June 2009

Design Forum

DESIGN FORUM papers range from design case studies to presentations of new methodologies to speculations about emerging design trends. They vary from 2500 to 12,000 words (where a figure or table counts as 200 words). Following informal review by the Editors, they may be published within a few months of the date of receipt. Style requirements are the same as for regular contributions (see inside back cover).

Design of an Electric Propulsion System for a Quadrotor Unmanned Aerial Vehicle

Michael J. Stepaniak[*]
Air Force Institute of Technology, Wright–Patterson Air Force Base, Ohio 45433
and
Frank van Graas[†] and Maarten Uijt de Haag[‡]
Ohio University, Athens, Ohio 45701

DOI: 10.2514/1.38409

A quadrotor unmanned aerial vehicle has been developed at Ohio University's Avionics Engineering Center for use as a navigation sensor testbed. The quadrotor was designed with a 10 lb payload capacity, transforming what has typically been a lightweight airframe into a more robust platform. Specific design considerations included the characteristics of high-power brushless motors and electronic speed controllers, the variation of motor rotational losses with frequency, and the impact of heat dissipation within the battery packs. Simple feedback loops were sufficient to stabilize the platform. An accounting of the component efficiencies allowed for effective mission planning based on the desired payload. The quadrotor, with a demonstrated ability to lift up to 10.6 lb, provides a convenient way to flight-test new sensor technology.

Nomenclature

B = flux density
B_m = sinusoidal peak flux density
C_b = battery capacity
C_e = effective capacity coefficient
C_Q = torque coefficient
D = flight duration
f = motor control-signal frequency
H_m = motor angular momentum
I = current
$I_{x,y,z}$ = quadrotor moment of inertia
J_m = motor moment of inertia
K_b = back electromagnetic force constant
K_t = torque constant
K_v = voltage constant
$K_{1,2}$ = rotational loss coefficients
k = Steinmetz core loss coefficient
k_a = anomalous core loss coefficient
k_b = battery discharge factor
k_{ch} = hysteresis correction factor
k_e = eddy-current coefficient
k_h = hysteresis coefficient
l_m = motor moment arm
N = motor speed
N_p = number of motor poles
P = power
Q = torque
R = resistance
$r_{1,2,3}$ = internal resistance coefficients
T = thrust
V = voltage
W_c = motor core mass
α, β = Steinmetz core loss coefficients
θ = pitch angle
ϕ = roll angle
ψ = yaw angle
Ω = motor speed

Subscripts

a = armature
b = battery
c = core loss
e = electronic speed controller
f = full-charge
m = motor
o = no load
ps = power supply
r = rotational loss
ref = reference
rms = root mean square
t = total
0 = nominal

Received 4 June 2008; revision received 13 October 2008; accepted for publication 8 November 2008. This material is declared a work of the U.S. Government and is not subject to copyright protection in the United States. Copies of this paper may be made for personal or internal use, on condition that the copier pay the $10.00 per-copy fee to the Copyright Clearance Center, Inc., 222 Rosewood Drive, Danvers, MA 01923; include the code 0021-8669/09 $10.00 in correspondence with the CCC.

[*] Assistant Professor, Department of Electrical and Computer Engineering. Member AIAA.

[†] Professor, Avionics Engineering Center.

[‡] Professor, Avionics Engineering Center. Member AIAA.

Introduction

A ROTARY-WING helicopter has considerable advantages over a fixed-wing airplane for many applications. For example, the vertical takeoff and landing capability greatly facilitates launch and recovery within a minimal footprint and without the logistical overhead of launching mechanisms such as catapults or rails. The slower forward speeds of a helicopter are advantageous in congested areas, such as the urban environment, or indoors, where obstacle avoidance is a primary concern and the turn radius of a fixed-wing aircraft would be prohibitively large. Also, the helicopter's ability to hover over a fixed point is advantageous when performing surveillance or imagery operations.

Furthermore, a quadrotor design affords additional advantages over a single-rotor helicopter. For example, the complexity of an articulated rotor hub and gear box is replaced by simple fixed-pitch propellers. Using counter-rotating propellers to balance the reaction torques eliminates the need for a tail rotor, minimizing the contact hazard and facilitating operations in confined environments. Safety can be further enhanced by enclosing the four rotors within a protective hull. One environment for which the rotary-wing quadrotor is particularly well suited is in a cluttered urban environment.

A number of sensor-related research efforts are underway at Ohio University's Avionics Engineering Center (AEC), to include wide baseline Global Positioning System attitude determination, ground imaging radar, video-based collision avoidance, and the use of laser detection and ranging (LADAR) for precision navigation. Flight testing of these systems has historically been accomplished using a variety of fixed-wing aircraft, ranging from a Brumby unmanned aerial vehicle to a large DC-3 testbed. The availability of a quadrotor platform with sufficient payload to carry these and other prototype sensors would greatly reduce the cost and logistical overhead necessary to collect airborne data. However, quadrotor UAV designers have generally focused on small designs with limited payloads that are not able to lift the larger sensors planned for this platform.

Therefore, the AEC began an effort to develop a quadrotor with a significantly greater payload (Fig. 1). The resulting platform supports a 10 lb payload, which is 3 times the capacity of similar quadrotors. This paper details the design considerations related to the propulsion system, the method used to stabilize the platform, and the flight-test results.

Background

Quadrotors have a distinguished early career in manned applications. The first helicopter to achieve flight was a quadrotor design, the tethered Bréguet-Richet No. 1 in 1907 [1]. In the 1920s, subsequent quadrotors achieved time and distance records for helicopter flights [2], and one of these, Etienne Oemichen's record-breaking quadrotor, continued on to fly over 1000 test flights [1]. In the 1920s, the U.S. Army Air Corps even tested a quadrotor built by George de Bothezat at McCook Field, predecessor to Wright–Patterson Air Force Base, Ohio, though the quadrotor was never funded for production [1]. An unmanned quadrotor appeared three decades later with Piasecki Aircraft Corporation's PA-4 Sea Bat: a drone intended for U.S. Navy shipborne operations, the Sea Bat succeeded in achieving tethered flight.[§] Around the same time, the Convertawings Model A quadrotor was successfully flown in New York [1]. Then, except for experimental tilt-rotors, the quadrotor design would fall out of favor for the next half-century.

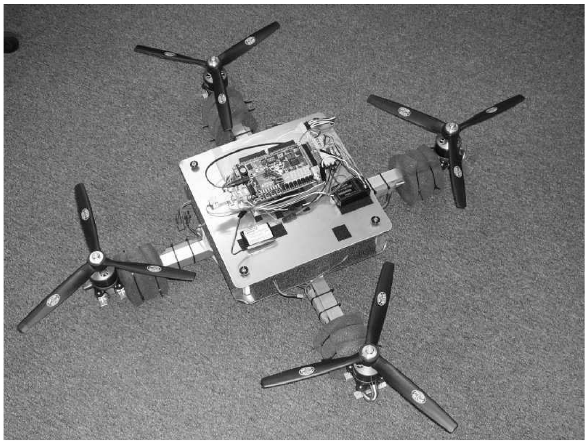

Fig. 1 AEC quadrotor.

In the last decade there has been a resurgence of interest in the quadrotor configuration for unmanned aerial vehicles (UAVs). Initial research into quadrotor UAVs were spurred by the introduction of radio-controlled models intended for hobbyists. Quadrotors have been marketed for surveillance [3,4] and some of the lightweight quadrotors have also been modified for research in control theory [5–8]. These platforms have a limited payload capacity (approximately 4 oz for the Draganflyer III [9]), which is sufficient for controls research but not able to support heavier sensors.

A few organizations have pursued original designs. The smallest is Stanford University's diminutive Mesicopter, a microelectromechanical system quadrotor that also achieved tethered flight [10]. A larger platform, the X4-Flyer designed and built at the Australian National University, is intended to serve as a rugged robotics testbed and boasts a 1 kg payload. An improved X4-Flyer Mark II featured custom-built rotor blades on a sprung teetering rotor hub to address instabilities related to blade flapping, but "chaotic semistable" behavior when flown tethered precluded advancing to free flight [11,12].

Two smaller quadrotors have been designed and flown for modeling and controls research: the French-built X4-Flyer [13] (no relation to the larger Australian vehicle of the same name) and the lightweight OS4 built by the Swiss Federal Institute of Technology [14]. A calamity-observation quadrotor built at the Korea Institute of Industrial Technology has over 3 lb of usable payload. Equipped with 13 infrared and ultrasonic range sensors, an inertial navigation system, and a video camera, the quadrotor weighs 2.4 lb without batteries [15]. Used for cooperative controls research, the STARMAC II also supports a 3 lb payload and has been tested with various sensors to include a stereo vision camera and a low-power laser range finder [16].

Brushless Motor

A 10 lb payload is enabled by efficient, high-power, brushless, direct-current (dc) motors coupled with high-energy-density lithium-polymer batteries. Brushless motors replace the field windings with permanent magnets located on the rotor and move the armature windings to the stator. In this manner, the need for brushed mechanical commutation is eliminated, reducing noise and electromagnetic interference due to arcing and gaining some efficiency. Maintenance is also greatly reduced, as there are no brushes to be to replaced. A disadvantage of the brushless motor is the need to perform the commutation electronically in a separate unit, as will be discussed in the following section.

A relatively new type of brushless dc motor uses an outrunner configuration, in which the base and armature windings are fixed to the airframe and the outer case spins as part of the rotor [17]. In this manner, a greater number of permanent magnets can be attached to the rotor, resulting in a magnetic gearing effect [18] that provides a greater amount of torque at low speeds without the need for mechanical gearing. High-power outrunner motors were therefore selected to directly drive the 14-in-diam propellers, eliminating the complexity and weight associated with gear boxes.

In an ideal direct-current motor, the desired motor speed is set by controlling the armature voltage and allowing the motor to draw sufficient current to drive the propeller. Real efficiency, however, is decreased by electrical and mechanical losses, one of which is the copper loss. Accounting for the power dissipated as heat in the

---

[§] Data available online at http://www.piasecki.com/pa-4.htm [retrieved 1 September 2008].

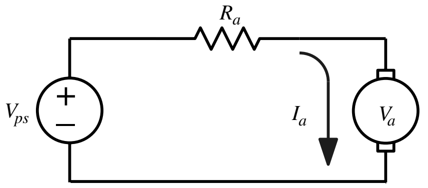

Fig. 2 Basic motor model.

armature windings, copper loss is modeled as an armature resistance R_a, as shown in Fig. 2, with the corresponding power loss in the armature:

$$P_a = I_a^2 R_a \tag{1}$$

Note that the inductance of the armature has been omitted from this model, as the electrical time constant will be insignificant compared with the mechanical time constant [19]. A second loss that impacts efficiency, the iron or core loss, will be considered later.

Without the ability to vary gearing to achieve the desired torque for a given motor speed, however, the motor selection is more critical. The governing relationships between motor speed and torque, N and Q, respectively, and armature voltage and current, V_a and I_a, respectively, are

$$Q = K_t I_a \tag{2}$$

$$N = K_v V_a \tag{3}$$

where K_t and K_v are the torque and voltage constants, respectively. For motors used in remote control applications, these constants are typically published with units of $\mathrm{oz} \cdot \mathrm{in.}/A$ and rpm/V, respectively. From Eqs. (2) and (3), the product of K_v and K_t is the ratio of mechanical power to electrical power, and with consistent units, the ratio would be unity. In the units of $\mathrm{oz} \cdot \mathrm{in.}/A$ and rpm/V, the relationship becomes

$$K_v K_t = 1352 \tag{4}$$

The implication of the inverse relationship between K_v and K_t is that a motor that spins fast (high K_v) will need to draw a high current to produce a given amount of torque (low K_t), and vice versa. The goal then is to select a motor with a pair of constants that will generate the desired thrust (a function of motor speed) at a current draw, proportional to torque, that is within the specified limits of the motor. Because the relationship between thrust and torque is governed by the design of the propeller used, a propeller model must be matched to the motor model to quantify the performance of a given motor. Without published aerodynamic coefficients, data collected from a thrust test stand can be used to generate the propeller model.

Electronic Speed Controller

A complicating factor with the use of brushless motors is the introduction of an electronic speed controller (ESC), a device external to the motor that electronically performs the commutation achieved mechanically in brushed motors. The ESC converts the battery pack's dc voltage to a three-phase alternating signal that is synchronized to the rotation of the rotor and applied to the armature windings. The motor speed is then proportional to the root-mean-square (rms) value of the armature voltage and is set by the ESC in response to a pulse-width-modulated control signal. The relationship between the control signal and the voltage level is not necessarily linear and must be confirmed experimentally. For example, the ESC units used for this quadrotor could be programmed to provide either a linear power response or a linear speed response.

Direct measurement of the three-phase voltage or current can be made with a true rms meter with sufficient bandwidth and current limits only if it is known whether the armature windings are connected in a wye or a delta configuration. An alternate approach is to model the ESC as shown in Fig. 3. Accounting for the power consumed by the electronics, P_e, the power available to the motor can be determined from the power supply voltage and current as

$$P_m = V_{\mathrm{ps}} I_{\mathrm{ps}} - P_e \tag{5}$$

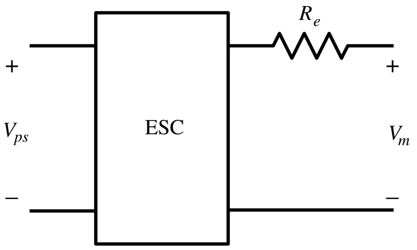

Fig. 3 Electronic speed controller model.

Power consumed by the ESC is expected to be negligible under normal operating conditions; however, this loss may be a factor when collecting measurements under low power, such as when calculating motor core loss with no load. Assumed constant, P_e can be determined from Eq. (5) by applying power to the ESC without connecting the motor leads. The resistor R_e, shown in Fig. 3, represents the resistance of the solid state switches and the value is provided by the manufacturer.

Modeling Core Loss

An improvement over the typical model can be made by accounting for the core loss in the motor. Core loss stems from the heat loss due to eddy currents that are induced in the iron core of the motor and also from the hysteresis of the magnetic field intensity in the core [20]. The core losses are difficult to characterize analytically, as they are a function of the materials used and the physical configuration of the motor. One method to estimate the core loss is to measure the power required to turn the motor without the propeller attached. Neglecting mechanical and copper losses, the power required can then be attributed to core loss [21], and the corresponding no-load current I_o can be incorporated into the motor model, as in Fig. 4 [22]. However, this no-load current model is suitable only for operating speeds near the no-load speed of the motor [21], which was measured at 10,500 rpm. As a testbed platform that supports a variety of payload configurations, the takeoff weight of the AEC quadrotor can range from 16.5–26.5 lb, corresponding to an operating range for the motor of 50–70% of the no-load motor speed, as determined using a thrust test stand. With a wide variation in operating speed, the adequacy of the no-load current model must be considered.

Variation in Core Loss as a Function of Motor Speed

Several models for core loss are available that account for frequency variation. The simplest, the Steinmetz equation, is a nonlinear model that describes core loss as a function of frequency and magnetic flux intensity:

$$P_c = k f^\alpha B_m^\beta \tag{6}$$

where f and B_m are the frequency and peak flux density, respectively, for sinusoidal magnetic fields, and k, α, and β are constants specific to the magnetic material. The three constants can be empirically matched to data collected in various frequency bands, providing a fair approximation to the actual values.[¶]

A generalization of the Steinmetz equation has been successfully applied to nonsinusoidal signals and might be applicable if the Steinmetz coefficients were known [23]. Other models account separately for the hysteresis and eddy current. In addition, a third term can also be introduced to account for residual excess losses.

[¶] Data available online at http://www.mag-inc.com/ferrites/ferrites.asp [retrieved 18 March 2009].

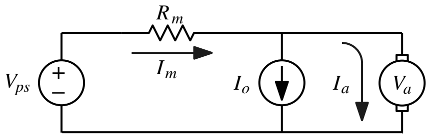

Fig. 4 No-load current model.

For a nonsinusoidal source, as in the case of a brushless motor, an improved model for specific core loss is [24]

$$\frac{P_c}{W_c} = k_{\mathrm{ch}} k_h f B_m^{\alpha} + \frac{k_e}{2\pi^2}\left(\frac{dB}{dt}\right)^2_{\mathrm{rms}} + \frac{k_a}{(2\pi^2)^{\frac{3}{4}}}\left(\frac{dB}{dt}\right)^{1.5}_{\mathrm{rms}} \tag{7}$$

where k_{ch} is an empirical correction factor for minor hysteresis loops; k_h, k_e, and k_a are the hysteresis, eddy current, and anomalous loss coefficients, respectively; α is a constant determined by the material properties; and W_c is the mass of the core material. Applying this model is complicated by the fact that recent research has shown that the anomalous loss term may be superfluous and that the loss coefficients vary as a function of frequency and flux density [25]. In addition, although motors using laminated silicon steel are generally expected to have very small eddy currents [22], rapid changes in the flux density will affect both the eddy-current term and the anomalous loss term. In fact, significant pulses in the armature current coinciding with the current switching by the electronic speed controller have been shown to have a large impact on core loss [26].

Empirical Model for Rotational Loss

Determination of the coefficients in Eq. (7) is beyond the scope of this project. Instead, an empirical model generated from measured data is used. Based on the general forms of Eqs. (6) and (7) and omitting the anomalous loss term, the rotational loss, including the core loss, is expected to have the following relationship:

$$P_r = K_1 N + K_2 N^2 \tag{8}$$

where K_1 and K_2 are constants. The procedure used to collect the data necessary to determine these constants is described next.

With no load attached and the control signal to the electronic speed controller increased, the current draw initially rises with the motor speed but quickly reaches a steady-state value. Data necessary to determine the core loss frequency dependence are therefore concentrated in the lower range of the motor control signal. With no load applied, the rotational power loss in the armature, P_r, can be calculated from Fig. 5 as

$$P_r = P_{\mathrm{ps}} - P_e - I_r^2 R_m \tag{9}$$

where a composite motor resistance $R_m = R_a + R_e$ is defined for convenience; P_{ps} is the power supplied to the electronic speed controller, which can be measured directly or calculated as $P_{\mathrm{ps}} = I_{\mathrm{ps}} V_{\mathrm{ps}}$; and I_r is the motor current necessary to overcome the rotational loss. The second term in Eq. (9) takes into account the copper loss, a term that is expected to be negligible because the no-load armature currents will be small. Also, this method does not distinguish between core loss and mechanical loss, as the field in a permanent magnet motor cannot be electrically removed to isolate the mechanical losses. An option not pursued in this research is to determine the mechanical losses by using a dummy motor, in which the permanent magnets have been destructively removed from the rotor [26]. Instead, the rotational loss calculated includes both core and mechanical losses.

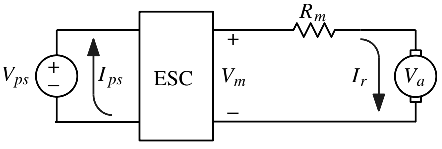

Fig. 5 ESC and motor.

An alternate expression for the power consumed by the armature is

$$P_r = I_r V_a \tag{10}$$

The motor current can then be calculated by equating the two expressions for rotational loss [Eqs. (9) and (10)]:

$$I_r^2 R_m + I_r V_a + (P_e - P_{\mathrm{ps}}) = 0 \tag{11}$$

Substituting Eqs. (3) and (5) into Eq. (11) yields the quadratic equation

$$I_r^2 R_m + I_r\left(\frac{N}{K_v}\right) + (P_e - P_{\mathrm{ps}}) = 0 \tag{12}$$

where the one solution that is physically realizable represents the armature current required to overcome the core and mechanical losses:

$$I_r = \frac{-(N/K_v) + \sqrt{(N/K_v)^2 - 4(P_e - P_{\mathrm{ps}})R_m}}{2R_m} \tag{13}$$

From Eqs. (3) and (10), the rotational loss is

$$P_r = I_r N / K_v \tag{14}$$

Figure 6 shows the difference between the constant-no-load current model and the rotational loss data collected. After using regression to determine the model constants, the speed-dependent model presented in Eq. (8) is found to aptly describe the data collected. For the constant-no-load current model depicted, I_o was measured at an applied voltage of 10 V to match the published specification for that motor. Although there is a difference between the two models, the models are a close match in the operating region of 5000–7500 rpm. Furthermore, it will be shown that the rotational losses, which dominate at lower speeds, play a diminishing role at greater speeds. Therefore, the use of the no-load current model is sufficient.

As with the no-load current model, the motor speed is directly proportional to the voltage across the armature, and so it is sufficient to model the rotational loss in terms of the associated current I_r, which can be calculated by dividing the power in Eq. (8) by the armature voltage from Eq. (3) to get

$$I_r = K_1 K_v + K_2 K_v N \tag{15}$$

This current is then incorporated into the motor model, as shown in Fig. 7.

Lithium-Polymer Batteries

Lithium-polymer batteries are well suited for the quadrotor, due to their high specific energy. These batteries also have a low internal resistance which can be considered negligible for some applications. For high-power applications, however, the loss associated with this resistance, dissipated as heat in the battery pack, accounts for a significant portion of the power budget and must be considered. The impact of the internal resistance is evident in Fig. 8, which plots data for increasing thrust measurements. The pulse-train appearance

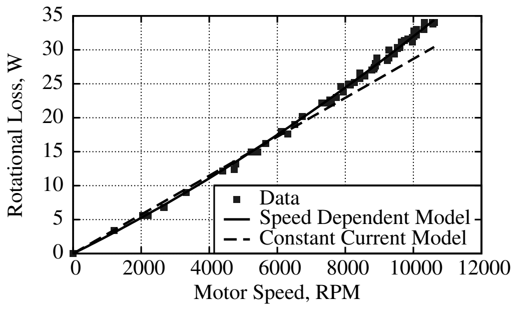

Fig. 6 Comparison of rotational loss models.

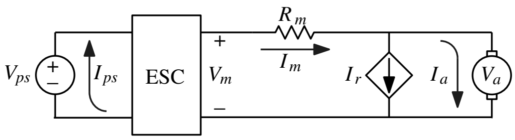

Fig. 7 Frequency-dependent core loss model.

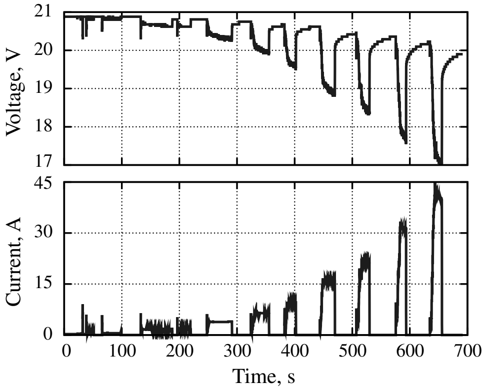

Fig. 8 Variation in battery voltage due to internal resistance.

results from spacing the test points to allow the open-circuit battery voltage to approach the resting voltage. The difference between the resting voltage and the voltage under load, ΔV_b, corresponds to the voltage drop across the battery pack's internal resistance:

$$R_b = \Delta V_b / I_b \tag{16}$$

where I_b is the measured current under load.

Interestingly, when the internal resistance is plotted as a function of current (Fig. 9), the resistance actually decreases with current for moderate-to-heavy loads. This is consistent with an analytical expression for the internal resistance of a single lithium-ion cell [27]:

$$R_b = r_1(t) + \frac{r_2(t) \ln I_b}{I_b} + \frac{r_3(t)}{I_b} \tag{17}$$

where coefficients r_1, r_2, and r_3 are functions of temperature t. Although this ohmic overpotential increases with temperature, the terminal voltage is also limited by the concentration overpotential, which decreases with temperature [27]. Ignoring temperature effects, Eq. (17) can then be used to model the resistance of the quadrotor battery packs using constant coefficients. Note that the model is ill-behaved for small currents but adequately describes the region of interest, as shown in Fig. 9. Also, the model serves only as a lower bound, as the internal resistance will increase as the cells age.

Propellers

With four independent rotors, flight control can be established without the use of cyclic pitch, and therefore simple fixed-pitch propellers can be employed. With rotors arranged in counter-rotating pairs, sets of rotors that are matched in terms of twist and airfoil are desirable. Fortunately, pusher propellers, normally mounted at the back of a fixed-wing aircraft, can be applied, because the brushless motors are easily reversed by merely swapping two of the three motor leads. Although selection is limited, large-diameter propellers are available in matching pusher and tractor configurations.

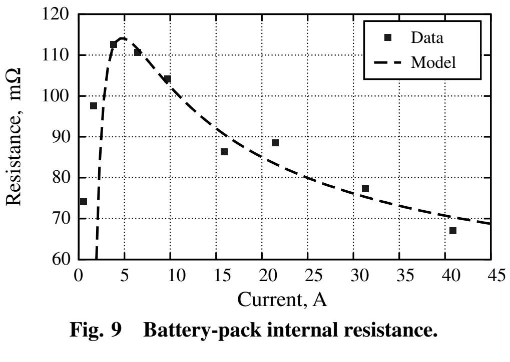

Fig. 9 Battery-pack internal resistance.

Characterization of the propulsion system required measurement of thrust data collected, along with the electrical motor parameters. The thrust test-stand configuration for this project consisted of a hinged lever with the motor mounted on the free end. A pusher propeller attached to the motor shaft provided a downward directed force that was measured using a digital scale. No special provisions were made to account for the airflow, which limited the maximum thrust that could be measured. At higher throttle settings with an exit velocity of 52 mph, the induced airflow circulated about the room and corrupted the data by impinging on the test stand. Data collected were sufficient to characterize the normal range of operation based on current limits within the motor. Measurements with a larger propeller, without having to rely on an extrapolated model, would require a better ability to control the airflow during the data runs.

A suitable power supply capable of providing nearly a kilowatt of power to drive the motor and propeller was not available. Instead, a five-cell lithium-polymer battery pack provided the necessary power at a nominal voltage of 18.5 V. Expected current levels exceed the capability of typical laboratory in-line meters, and so the battery voltage and current were collected using an Eagle Tree data logger that was placed in line with the battery cable and provided both current and voltage readings. Motor speed was calculated from the frequency of the three-phase voltage measured at one of the motor leads. The relationship of this frequency to the motor speed is

$$N = \frac{60f}{N_p/2} \tag{18}$$

Because the data logger provides the terminal voltage on the battery, it is not necessary to account for the internal resistance of the battery, and the model shown in Fig. 7 is sufficient. The current drawn by the motor can be calculated in an analogous manner as for I_r:

$$I_m = \frac{-(N/K_v) + \sqrt{(N/K_v)^2 - 4(P_e - P_{\mathrm{ps}})R_m}}{2R_m} \tag{19}$$

Then, accounting for the current associated with rotational loss, the armature current is

$$I_a = I_m - I_r \tag{20}$$

and the torque on the motor shaft is calculated using Eq. (2). With the motor speed and shaft torque known, nondimensional thrust and torque coefficients for the propeller can be determined using [28]

$$C_T = \frac{T}{\rho \pi R^4 \Omega^2} \tag{21}$$

$$C_Q = \frac{Q}{\rho \pi R^5 \Omega^2} \tag{22}$$

Whereas the thrust and torque coefficients vary with the ratio of the freestream velocity to the propeller speed, in a constant altitude hover, the freestream velocity is zero and the two coefficients can be approximated as constants. As a sensor testbed, the flight profiles for the AEC quadrotor are expected to be benign, with only limited deviations from the hover. As a result, the thrust and torque can be modeled as proportional to the square of the motor speed, and the coefficients can be determined using regression.

Platform Stabilization

The quadrotor is configured with two pairs of counter-rotating propellers arranged such that opposing motors spin in the same direction. Pitch and roll angles are controlled through the application of differential thrust along one axis. Increasing thrust from one motor while decreasing the thrust from the opposing motor results in a pitch or roll moment without a significant impact on altitude or yaw. Applying differential torque between the counter-rotating pairs, on the other hand, controls the yaw rate. Specifically, by increasing thrust to one pair of motors while decreasing thrust to the counter-rotating motors, the total thrust can be maintained, preserving altitude, and the difference in reaction torque induces a yawing motion.

In stabilizing the attitude of the quadrotor, only the rotational dynamics need to be considered. For a symmetric quadrotor, where $I_x = I_y$, these nonlinear dynamics have been shown to be [29]

$$\begin{aligned}\ddot{\phi} &= \frac{(I_y - I_z)}{I_x}\dot{\theta}\,\dot{\psi} - \frac{H_m}{I_x}\dot{\theta} + \frac{l_m}{I_x}(T_4 - T_2)\\ \ddot{\theta} &= \frac{(I_z - I_x)}{I_y}\dot{\phi}\,\dot{\psi} + \frac{H_m}{I_y}\dot{\phi} + \frac{l_m}{I_y}(T_1 - T_3)\\ \ddot{\psi} &= \frac{1}{I_z}(Q_2 + Q_4 - Q_1 - Q_3)\end{aligned} \tag{23}$$

where l_m is the moment arm of the motors, H_m is the total angular momentum of the motors and propellers, $I_{x,y,z}$ are the moments of inertia, and the numerical subscripts denote the component of thrust or torque associated with of the four motors. Linearizing about a hover, where $\dot{\phi} = \dot{\theta} = \dot{\psi} = H_m = 0$, results in

$$\begin{aligned}\ddot{\phi} &= \frac{l_m}{I_x}(T_4 - T_2) \qquad \ddot{\theta} = \frac{l_m}{I_y}(T_1 - T_3)\\ \ddot{\psi} &= -\frac{1}{I_z}(Q_2 + Q_4 - Q_1 - Q_3)\end{aligned} \tag{24}$$

where the nominal thrust of each motor is equivalent to one-fourth of the vehicle weight. The first-order model used for the motors is [19]

$$\frac{\Omega(s)}{V_m(s)} = \frac{K_b/R_m J_m}{s + (1/J_m)(D_m + (K_b^2/R_m))} \tag{25}$$

where K_b is the motor back electromagnetic force constant, D_m is the equivalent system damping, and J_m is the moment of inertia of the motor and propeller. From the voltage constant, K_b can be calculated as

$$K_b = \frac{60}{2\pi K_v} \tag{26}$$

The moment of inertia of the motor and propeller was determined experimentally. The true damping varies with motor speed but can be approximated by the damping at the nominal operating point:

$$D_m = \frac{Q_0}{\Omega_0} = C_Q R^3\sqrt{\frac{T_0 \pi \rho}{C_T}} \tag{27}$$

Stabilization is accomplished using classical control, as shown in the block diagrams for pitch and yaw (Fig. 10). The reference inputs θ_{ref} and $\dot{\psi}_{\text{ref}}$ are proportional to the stick position on the radio controller. Because of symmetry, the roll channel feedback loops and response are identical to the pitch channel. Inner-loop feedback from rate gyroscopes provides damping about all three axis, and a lead-compensated outer feedback loop for the pitch and roll channels provides the desired attitude tracking. The control loops operate at 50 Hz, corresponding to the frequency of the pulse-width-modulated reference signals generated by the radio receiver and the motor control signals sent to the electronic speed controllers. A Padé approximation for the digital sample and hold is incorporated.

The goal of the project was to provide a stabilized platform that could be easily flown remotely and not necessarily flown autonomously. Without additional aiding, the gyro drift errors preclude the vehicle from maintaining an absolute position without corrections from the pilot.

The values for the loop gains and lead compensator were chosen to achieve a satisfactory step response, simulated in Fig. 11 for the baseline takeoff weight of 16.5 lb. These gains can be adjusted, if required, based on takeoff weight and mass distribution of the planned configuration. Because the payloads are fixed during the course of a flight, there are no provisions for adjusting the gains in flight. However, the field-programmable gate array (FPGA) stores multiple sets of gains that can then be selected during preflight, allowing flights with multiple preplanned payloads without having to reprogram the FPGA.

Configuration

The basic airframe is a cross-shaped structure built from 1 in. square aluminum tubing. A square enclosure attached above the frame contains four battery packs and serves as a mounting surface for the electronics. There are 42 in. between the tips of opposing propellers, and the quadrotor weighs 16.5 lb without a payload. Other than the aluminum airframe, the quadrotor was built using off-the-shelf components.

Propulsion is generated by four Model Motors AXi 4120/18 brushless motors, each capable of generating over 8 lb of thrust when paired with 14 in. Master Airscrew MA1470T propellers. Power for each motor was supplied by a Thunder Power TP8000-5S4PL lithium-polymer battery pack with a current capacity exceeding the 55 A maximum rating of the motor. Weighing 1.75 lb per pack, each provides 8 Ah of capacity and a nominal voltage of 18.5 V. Speed control for the brushless motors is accomplished by Jeti Advance 70 Opto Plus electronic speed controllers.

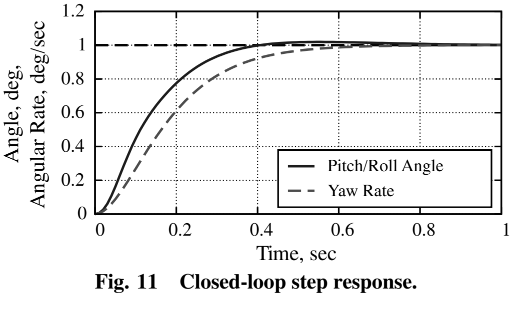

Fig. 11 Closed-loop step response.

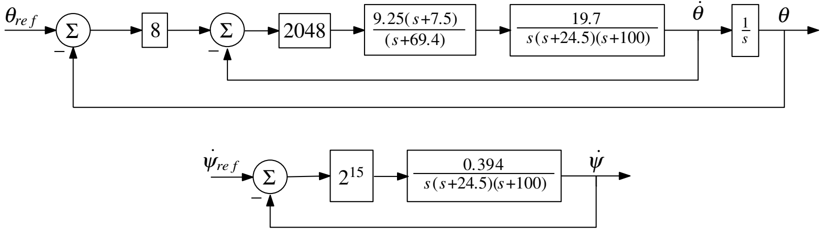

Fig. 10 Closed-loop block diagrams for pitch angle θ and yaw rate $\dot{\psi}$.

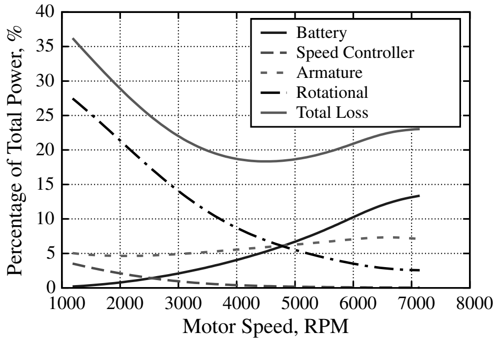

Fig. 12 Component losses as a percentage of total power.

Command of the quadrotor is accomplished using a Futaba remote control radio and receiver. Body angular rates from a Microstrain 3DM-GX1 gyro-enhanced orientation sensor are fed into a Spartan-3 FPGA. The FPGA hosts the navigation equations that track body attitude with respect to inertial space and also implements the feedback loops that stabilize the body. A small lithium-polymer battery pack and regulator supplies power to the electronics separately from the motor battery packs.

Results

Mission Planning

The power losses detailed in this paper are summarized in Fig. 12 as a percentage of the total power consumed from the battery. Under a light load, the loss is dominated by the rotational losses, but at greater leads corresponding to high motor speeds, the internal resistance of the battery plays an increasing factor, accounting for half of the losses. As anticipated in the Electronic Speed Controller section, the losses associated with the ESC are negligible.

The power loss associated with the internal resistance of the battery pack imposes two limitations on flight time. First, with over 100 W of power dissipated as heat under a 40 A load, the maximum operating temperature may be exceeded unless sufficient cooling is provided. In the lab, a 42 A load resulted in a battery pack approaching the 140°F limit after 10 min of continuous operation. As a result, the battery enclosure was modified to better facilitate passive cooling, and additional testing using the battery enclosure will be pursued.

The second limitation is the decrease in available battery capacity due to the internal power loss, which can account for over 13% of the power consumed. A chart such as Fig. 13 is a convenient tool that can be used to determine the resulting flight duration as a function of required thrust. The curve in the left chart represents the power required P_{ps}, based on the vehicle takeoff weight, and can be constructed from a conservation of power analysis of Fig. 7:

$$P_{\mathrm{ps}} = P_e + (I_r + I_a)^2 R_m + (I_r + I_a) V_a \tag{28}$$

where P_e is determined experimentally, as described earlier in this paper; I_r is modeled using Eq. (15), and I_a and V_a are calculated from Eqs. (2) and (3), respectively. Note that expressions for current and voltage require knowledge of the motor speed and torque, which are calculated from an adjusted nominal thrust using Eqs. (21) and (22), respectively. The adjustment to nominal thrust accounts for the loss in propeller efficiency when installed on the quadrotor. Figure 13 includes an 11% reduction in efficiency that was calculated by comparing flight-test data for a range of payloads with the data collected on the thrust test stand.

The power-required curve on the right side of the chart is calculated as

$$P_{\mathrm{ps}} = P_t - I_{\mathrm{ps}}^2 R_b \tag{29}$$

where P_t is the total power consumed from the battery. Total power is calculated as

$$P_t = V_f I_{\mathrm{ps}} \tag{30}$$

where V_f is the full-charge battery voltage and is equivalent to the number of cells in the battery pack multiplied by 4.1 V. The internal resistance of the battery, R_b, varies with the power supply current I_{ps} and is calculated using Eq. (17). The flight duration D in minutes is calculated as

$$D = \frac{60 V_0 C_b C_e}{V_f I_{\mathrm{ps}}} \tag{31}$$

where V_0 is the nominal voltage of the battery pack, equivalent to the number of cells in the battery pack multiplied by 3.7 V, C_b is the rated capacity of the battery pack in units of ampere hour, and C_e is an effective capacity coefficient. C_e is defined as the percentage of rated capacity available before the sudden rolloff in voltage at the end of the discharge curve.

In use, the left chart gives the total power required to hover as a function of vehicle weight. The right chart then provides the battery current for each motor and the flight duration that corresponds to that power level. Additionally, the power dissipated as heat in the four battery packs is graphically illustrated as the difference between the power-consumed and the power-required curves. As an example, the quadrotor with a 10 lb payload requires nearly 3 kW of power. This power level corresponds to 505 W dissipated as heat, a 42.5 A current draw, and over 9 min of flight.

Flight-Test Results

The adequacy of the derived model and the suitability of the stabilization algorithm was verified in simulation and then empirically confirmed using a buildup approach. In the first step, a motor was mounted at the free end of a hinged lever arm. This allowed the verification of the thrust model by comparing the throttle required with the throttle predicted to maintain a level attitude. Although the dynamics of the lever arm varied significantly from the quadrotor

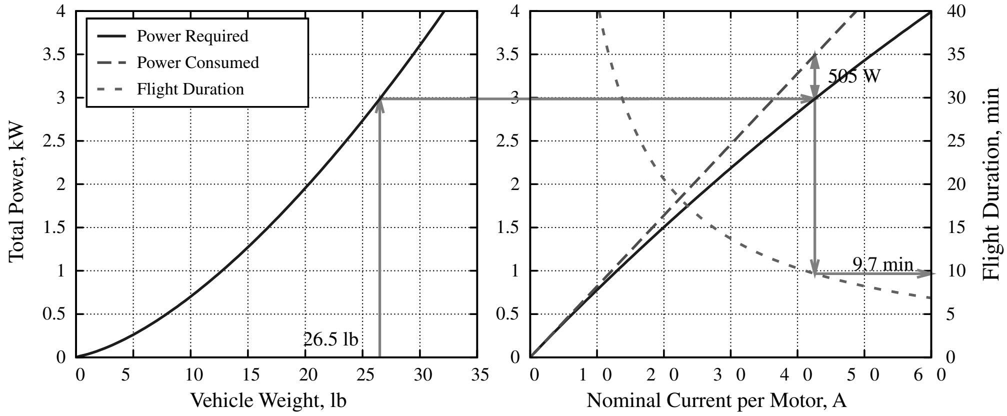

Fig. 13 Flight duration as a function of vehicle weight.

dynamics, this initial step also served to demonstrate proper implementation of the stabilization algorithm by tracking commanded angles.

The second step attached one arm of the quadrotor to a rotating shaft that allowed verification of the performance about a single axis. The attachment point used shims that allowed the axis of rotation to be aligned with the calculated center of gravity, preserving the quadrotor dynamics so that performance on this test fixture was representative of that anticipated in flight. The center of gravity was estimated using a point-mass model that accounted for the weight and location of each significant component. The proper alignment of the test fixture was confirmed by the lack of restoring moments about the shaft, regardless of attitude. With the quadrotor symmetrical about the pitch and roll axis and the yaw rate generally set to zero, this fixture facilitated the fine-tuning of the closed-loop gains to meet desired handling qualities.

The final test was free flight. The first attempt was unsuccessful, with the quadrotor showing a tendency to raise on one arm and eventually flip with increasing throttle. This led to a thorough review of the stabilization algorithm and its implementation on the FPGA. In addition, the variation between motors was considered, because this design does not use closed-loop control to assure matched motor speeds. With no anomalies noted, a second attempt at free flight was attempted using a launch platform to increase the distance between the rotors and the ground. The platform was constructed using wire mesh to minimize the disturbance to the airflow, and this launch method proved satisfactory, as the quadrotor launched readily on the second attempt without any modifications to the control law (Fig. 14). The exact cause of the initial upset during takeoff is unresolved, though ground effect may be a contributing factor.

Subsequent flights have flown with a carbon-fiber frame that attaches beneath the quadrotor. This frame serves as both a protective structure for the payload and as landing struts, eliminating the need for the launch platform. Specifically, the quadrotor has flown with 0, 3.1, 4.7, 6.1, and 10.6 lb payloads, with each flight using the same set of gains in the control laws. Although a complete characterization cannot be completed until the telemetry system is implemented, pilot feedback indicates that handling qualities improved as the payload increased up to 6.1 lb, followed by a decrease in performance at maximum payload. Overall, the quadrotor has demonstrated the ability to lift payloads up to 10.6 lb and exhibits excellent stability and flying qualities when flown with a 6.1 lb payload representative of the LADAR shown in Fig. 15.

Fig. 14 Initial flight configuration without the carbon-fiber frame.

Fig. 15 Line-scan LADAR mounted within the carbon-fiber frame.

Conclusions

The quadrotor design was successfully scaled up to serve as a testbed platform that can carry a significant payload. A method of modeling rotational loss as a function of motor speed was introduced but found to have no significant advantages in the operating region for this quadrotor. Power dissipation within the battery packs due to internal resistance, on the other hand, was found to be significant and a limiting factor in determining flight duration in terms of both temperature rise and power consumed. Based on successful flight tests, classical control theory proved sufficient to stabilize the quadrotor's attitude for low dynamic flight. With a 10 lb payload capacity, this quadrotor provides the Avionics Engineering Center with a new capability for testing airborne sensors.

Acknowledgments

This sensor platform supports theoretical research partially funded by the U.S. Air Force Office of Scientific Research (Jon Sjogren, Program Manager). The authors are grateful to Caleb White for designing the airframe and providing valuable experience to the project. The views expressed in this paper are those of the authors and do not reflect the official policy or position of the U.S. Air Force, the U.S. Department of Defense, or the U.S. Government.

References

[1] Gablehouse, C., *Helicopters and Autogiros*, J. B. Lippencott, Philadelphia, 1969.

[2] Fay, J., *The Helicopter*, 3rd ed., David & Charles, North Pomfret, VT, 1976.

[3] Marks, P., "Miniature Spy Helicopter Aims to Hover Unheard," *New Scientist*, Vol. 180, No. 2424, Dec. 2003, p. 27.

[4] Stafford, N., "Spy in the Sky," *Nature*, Vol. 445, No. 22, Feb. 2007, p. 808.

[5] Chen, M., and Huzmezan, M., "A Simulation Model and H_∞ Loop Shaping Control of a Quad Rotor Unmanned Air Vehicle," *Proceedings of the IASTED International Conference on Modelling, Simulation and Optimization*, ACTA Press, Calgary, Canada, July 2003, pp. 320–325.

[6] Castillo, P., Dzul, A., and Lozano, R., "Real-Time Stabilization and Tracking of a Four-Rotor Mini Rotorcraft," *IEEE Transactions on Control Systems Technology*, Vol. 12, July 2004, pp. 510–516. doi:10.1109/TCST.2004.825052

[7] Tournier, G. P., Valenti, M., How, J. P., and Feron, E., "Estimation and Control of a Quadrotor Vehicle Using Monocular Vision and Moiŕe Patterns," AIAA Guidance, Navigation, and Control Conference, Keystone, CO, AIAA Paper 2006-6711, Aug. 2006.

[8] Altuğ, E., and Taylor, C., "Vision-Based Pose Estimation and Control of a Model Helicopter," *Proceedings of the IEEE International Conference on Mechatronics*, Inst. of Electrical and Electronics Engineers, Piscataway, NJ, June 2004, pp. 316–321. doi:10.1109/ICMECH.2004.1364458

[9] Homann, G., Rajnarayan, D. G., Waslander, S. L., Dostal, D., Jang, J. S., and Tomlin, C. J., "The Stanford Testbed of Autonomous Rotorcraft for Multi Agent Control (STARMAC)," *Proceedings of the 23rd Digital Avionics Systems Conference*, Vol. 2, Inst. of Electrical and Electronics Engineers, Piscataway, NJ, Oct. 2004, pp. 12.E.4-1–12.E.4-10.

[10] Kroo, L., and Kunz, P., "Development of the Mesicopter—A Miniature Autonomous Rotorcraft," *American Helicopter Society Vertical Lift Aircraft Design Conference*, AHS International, Alexandria, VA, Jan. 2000, pp. 1–9.

[11] Pounds, P., Mahoney, R., Gresham, J., Corke, P., and Roberts, J., "Towards Dynamically-Favourable Quad-Rotor Aerial Robots,"

Proceedings of the Australasian Conference on Robotics and Automation [CD-ROM], edited by N. Barnes and D. Austin, Australian Robotics and Automation Association, Dec. 2004.

[12] Pounds, P., Mahoney, R., and Corke, P., "Modelling and Control of a Quad-Rotor Robot," *Proceedings of the Australasian Conference on Robotics and Automation* [CD-ROM], edited by B. MacDonald, Australian Robotics and Automation Association, Dec. 2006.

[13] Guenard, N., Hamel, T., and Moreau, V., "*Dynamic Modeling and Intuitive Control Strategy for an 'X4-Flyer'*," *International Conference on Control and Automation*, Inst. of Electrical and Electronics Engineers, Piscataway, NJ, June 2005, pp. 141–146. doi:10.1109/ICCA.2005.1528106

[14] Bouabdallah, S., and Siegwart, R., "Full Control of a Quadrotor," *Proceedings of the International Conference on Intelligent Robots and Systems*, Inst. of Electrical and Electronics Engineers, Piscataway, NJ, 25 Oct.–2 Nov. 2007, pp. 153–158 .doi:10.1109/IROS.2007.4399042

[15] Park, S., Won, D. H., Kang, M. S., Kim, T. J., Lee, H. G., and Kwon, S. J., "RIC (Robust Internal-Loop Compensator) Based Flight Control of a Quad-Rotor Type UAV," *International Conference on Robots and Systems* [CD-ROM], Inst. of Electrical and Electronics Engineers, Piscataway, NJ, 2–6 Aug. 2005, pp. 3542-3547. doi:10.1109/IROS.2005.1545113

[16] Homann, G. M., Huang, H., Waslander, S. L., and Tomlin, C. J., "Quadrotor Helicopter Flight Dynamics and Control: Theory and Experiment," *AIAA Guidance, Navigation and Control Conference*, AIAA, Reston, VA, Aug. 2007, pp. 1–20.

[17] Bobay, D. P., and Young, G. C., "Motor with External Rotor," U.S. Patent 5,962,938, filed Oct. 5, 1999.

[18] Spooner, E., and Haydock, L., "Vernier Hybrid Machines," *IEE Proceedings B, Electric Power Applications*, Vol. 150, No. 6, Nov. 2003, pp. 655–662. doi:10.1049/ip-epa:20030909

[19] Nise, N. S., *Control Systems Engineering*, Benjamin/Cummings, New York, 1992.

[20] Holt, C. A., *Introduction to Electromagnetic Fields and Waves*, Wiley, New York, 1963.

[21] Chapman, S. J., *Electric Machinery Fundamentals*, 2nd ed., McGraw–Hill, New York, 1991.

[22] Boucher, R. J., *Electric Motor Handbook*, AstroFlight, Inc., Marina Del Rey, CA, 1994.

[23] Venkatachalam, K., Sullivan, C. R., Abdallah, T., and Tacca, H., "Accurate Prediction of Ferrite Core Loss with Nonsinusoidal Waveforms Using Only Steinmetz Parameters," *Proceedings of the IEEE Workshop on Computers in Power Electronics*, June 2002, pp. 36–41.

[24] Deng, F., "An Improved Loss Estimation for Permanent Magnet Brushless Machines," *IEEE Transactions on Energy Conversion*, Vol. 14, No. 4, Dec. 1999, pp. 1391–1395. doi:10.1109/60.815078

[25] Ionel, D. M., Popescu, M., Dillinger, S. J., Miller, T., Heideman, R. J., and McGilp, M. I., "On the Variation with Flux and Frequency of the Core Loss Coffiecients in Electrical Machines," *IEEE Transactions on Industry Applications*, Vol. 42, No. 3, May 2006, pp. 658–667. doi:10.1109/TIA.2006.872941

[26] Toda, K., Senda, K., and Ishida, M., "Eect of Material Properties on Motor Iron Loss in PM Brushless DC Motor," *IEEE Transactions on Magnetics*, Vol. 41, No. 10, Oct. 2005, pp. 3937–3939. doi:10.1109/TMAG.2005.854977

[27] Rong, P., and Pedram, M., "An Analytical Model for Predicting the Remaining Battery Capacity of Lithium-Ion Batteries," *IEEE Transactions on Very Large Scale Integration (VLSI) Systems*, Vol. 14, No. 5, May 2006, pp. 441–451. doi:10.1109/TVLSI.2006.876094

[28] Leishman, J. G., *Principles of Helicopter Aerodynamics*, 2nd ed., Cambridge Univ. Press, New York, 2006.

[29] Bouabdallah, S., Noth, A., and Siegwart, R., "PID vs LQ Control Techniques Applied to an Indoor Micro Quadrotor," *Proceedings of the IEEE International Conference on Intelligent Robots and Systems*, Vol. 3, Inst. of Electrical and Electronics Engineers, Piscataway, NJ, Sept. 2004, pp. 2451–2456. doi:10.1109/IROS.2004.1389776